GassDem: A MATLAB program for modeling the anisotropic seismic properties of porous medium using differential effective medium theory and Gassmann's poroelastic relationship☆

Eunyoung Kim[a], YoungHee Kim[a,*], David Mainprice[b]

[a] School of Earth and Environmental Sciences, Seoul National University, Seoul, 08826, Republic of Korea
[b] Géosciences Montpellier UMR CNRS 5243, Bâtiment 22, CC 060, Université de Montpellier, Place Eugène Bataillon, 34095, Montpellier Cedex 05, France

ARTICLE INFO

ABSTRACT

Seismic velocity and anisotropy are mainly controlled by the elastic components of rock microstructure. Here we present a MATLAB program, GassDem (Gassmann Differential effective medium), for modeling anisotropic seismic properties from rock microstructure using differential effective medium (DEM) theory and Gassmann's (1951) poroelastic relationship. Modeling provides a method to overcome the limitations of laboratory measurements, which are unable to reach realistic temperature and pressure conditions. DEM models a two-phase composite that consists of a background medium and inclusions. Components of the rock microstructure, such as porosity, crack geometry, and fluid type in the cracks, are considered to be inclusion properties in DEM theory. Gassmann's poroelastic relationship is used to calculate the elastic stiffness for fluid-saturated rocks. In the formulation of the DEM model, we achieve high numerical efficiency, particularly for inclusions with large aspect ratios, by taking the Fourier transform of the tensor Green's function and using the symmetry of the tri-axial ellipsoid to reduce the amount of integration. We provide examples of DEM modeling and a description for users to replicate the examples using the GassDem graphical user interface, or using a MATLAB script.

1. Introduction

Improvements in seismic methodology and the increase in the amount of seismic data from marine and continental experiments have led to high-resolution imaging of Earth's interior. For tomographic imaging, effective medium theory (EMT) has been used to interpret seismic velocity anomalies in the lithosphere (e.g., Huot and Singh, 2018; Kim et al., 2019; Mainprice, 1997). Self-consistent (SC) approximation is one of EMT methods, which models multi-phase composites in which each component is treated as an inclusion (Budiansky, 1965; Hill, 1965). Differential effective medium (DEM) theory is another of EMT methods, which models two-phase composites by incrementally adding the inclusion to the background (Bruner, 1976). DEM was used to model an effective medium consisting of basalt and seawater-filled cracks in order to estimate porosity variation in the upper oceanic crust beneath the Mid-Atlantic Ridge (Arnulf et al., 2011; Seher et al., 2010).

For sediments in the Mentawai forearc basin, Central Sumatra, the elastic moduli of an effective medium that is composed of sediment and either methane or seawater were computed using the SC approximation and then taken as an input for DEM to explore possible ranges of gas and fluid (Huot and Singh, 2018). A detailed description of the SC and DEM methods is given in Section 3.

Interpretations of seismic velocities are constrained by laboratory measurements on rock samples and calculations of the elastic constants of minerals (e.g., Almqvist and Mainprice, 2017; Paterson and Wong, 2005). However, elastic constant data to constrain seismic anisotropy, defined as the directional dependence of seismic velocity, at temperature and pressure (T-P) conditions of the crust and upper mantle are limited, and the experimental measurements needed to determine anisotropic elastic constants at high T-P remain a challenge (Almqvist and Mainprice, 2017). In addition, measurements using optical or electron microscopy are typically collected on 2-D surfaces, and sample

---

Fig. 1. Effective Medium tab of GassDem GUI. A two-component system of A and B can be constructed for DEM calculation. Fluid properties of compressibility (1/GPa), viscosity (Pa·s), Vp (km/s), and density (g/cm^3) are required for Gassmann's poroelastic relationship and attenuation estimation.

Fig. 2. Inclusion Shape and Orientation tab of GassDem GUI. Ellipsoid semi-axes lengths and the orientation of inclusion can be defined.

preparation is time-consuming, despite increasing speed of data acquisition (Almqvist and Mainprice, 2017). The lack of experimental data on seismic anisotropy due to the requirement for multiple measurement orientations can be overcome by modeling because it allows for full characterization of the elastic tensor of geological materials. Thus, modeling is essential for calculating the elastic constants of rocks at diverse T-P conditions and for understanding the origin of seismic anisotropy in rocks.

In this paper, we present a method that combines SC, DEM, and the poroelastic relationship of Gassmann (1951) to model the anisotropic seismic velocity of rocks, following modeling schemes given by Mainprice (1997). The original algorithm was written by Mainprice (1997) in FORTRAN77. We use the SC part of the FORTRAN77 code to calculate elastic moduli of the end-member background medium for
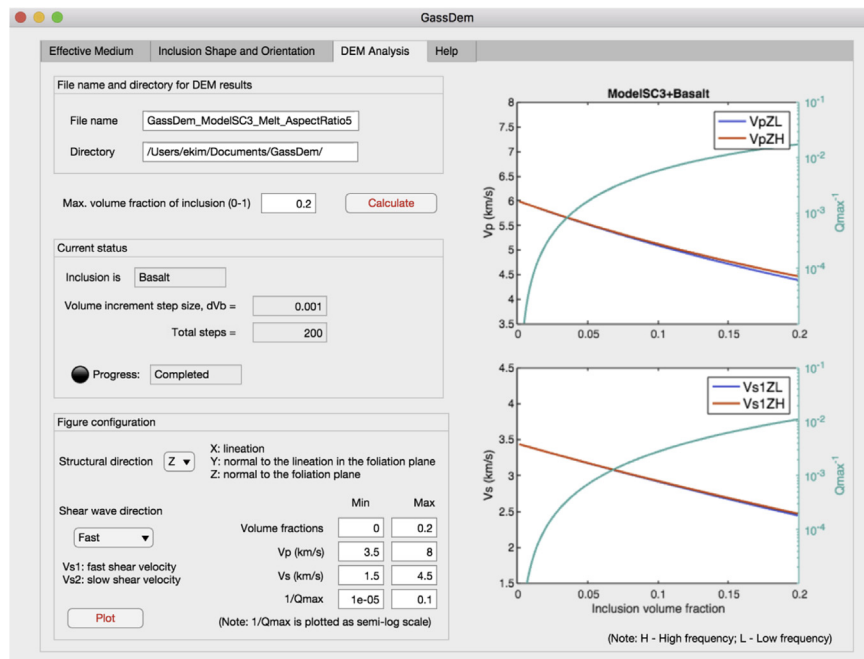
Fig. 3. DEM Analysis tab of GassDem GUI. File name and directory for DEM results can be set. A maximum of the inclusion volume fraction can be specified for DEM calculation. The outputs are saved as text files (*.txt). By setting the Figure configuration panel, *Vp*, *Vs*, and Q_{max}^{-1} are plotted for a given range of inclusion volume fraction.

DEM. We have translated the FORTRAN77 code for DEM and the poroelastic relationship of Gassmann (1951) into a MATLAB program (GassDem: Gassmann Differential effective medium). GassDem computes the elastic stiffness, seismic velocity, and maximum quality factor (Q_{max}^{-1}) of the effective medium. Prior to describing the modeling schemes in Section 3, we introduce the effects of several factors on the anisotropic seismic velocity and the feasibility of EMT methods to simulate the seismic properties based on the microstructural features of rocks in Section 2.

2. Microstructure and seismic properties

2.1. Pressure and seismic velocity

Calculation of the physical properties of rocks from microstructural information, such as crystal orientation, volume fraction, and grain shape, is important because it gives insight into the role of microstructure in determining the elastic properties. A combined approach of direct laboratory measurements and modeling enhances the interpretation of seismic data by identifying microstructural features (e.g., the distribution and geometric arrangement of crystals and cracked/fractured media) that affect the seismic properties of rocks (Almqvist and Mainprice, 2017; Barruol and Kern, 1996). Initial variations in *P*-wave velocity (*Vp*) with increasing pressure in laboratory measurements reflect the influence of crack opening or closing on the effective elastic stiffness of rocks, as almost all rock samples recovered on the Earth's surface contain microcracks. However, quantifying the crack density and geometry remains a difficult task using standard microscopy techniques (Griffiths et al., 2017; Kranz, 1983). Since cracks significantly affect the elastic properties of rocks, the nature of the crack population within a rock sample can be inferred by measuring *Vp* at appropriate pressure conditions (Carlson and Gangi, 1985). Microcracks tend to close with increasing pressure and open with decreasing pressure. The closure pressure (P_C) depends on the rock type and microcrack shape (Walsh, 1965). The initial trend in *Vp* with increasing pressure can provide insight into the variable crack density in the sample. The 3-D crack distribution in a sample can be indirectly

inferred by measuring the velocity drop caused by the presence of pores and open microcracks at atmospheric pressure on a spherical sample (Kern et al., 2015).

2.2. Effect of crack alignment on seismic anisotropy

Since microstructure significantly affects the elastic properties of rocks (Berryman and Berge, 1993), the role of microstructures and the geometrical arrangement of phases in the rock should be considered in calculating seismic velocities (Almqvist and Mainprice, 2017). If the calculation scheme considers grain shapes and orientations, the misfit between laboratory measurements and calculated velocities can be improved (e.g., Wenk et al., 2012). Among microstructural features, microcracks have considerable influence on seismic wave velocities, especially *Vp*, as well as the mechanical properties of rocks (Carlson and Gangi, 1985). For aligned ellipsoidal cracks, the main reduction in *Vp* occurs along the axis of symmetry, indicating that the variation in crack density, crack aspect ratio, or pore pressure causes significant variations in *Vp* and anisotropy (Anderson et al., 1974). Because the distribution of fluid-filled cracks and microcracks that are aligned by the contemporary stress field strongly influences seismic anisotropy and can cause shear-wave splitting, the analysis of shear waves propagating through the cracked rock can be used to monitor stress changes before earthquakes (e.g., Crampin, 1987; Pio Lucente et al., 2010). A microcrack can be empty or filled with fluid at some pore pressure, which can also influence the seismic wave velocities. For a solid matrix containing aligned ellipsoidal fluid-filled cracks, the bulk modulus of the pore fluid in the cracks significantly affects *Vp* for a propagation direction along the axis of symmetry (Anderson et al., 1974).

2.3. Prediction of seismic properties for in-situ state

Accurate single crystal elastic constants are paramount for predicting the elastic properties of the crust, yet much of this data for the rock-forming minerals in the continental crust are limited to measurements made at standard temperature and pressure (STP; atmospheric conditions) (Almqvist and Mainprice, 2017). High-T and high-P data

Antigorite 78% + Olivine 22%
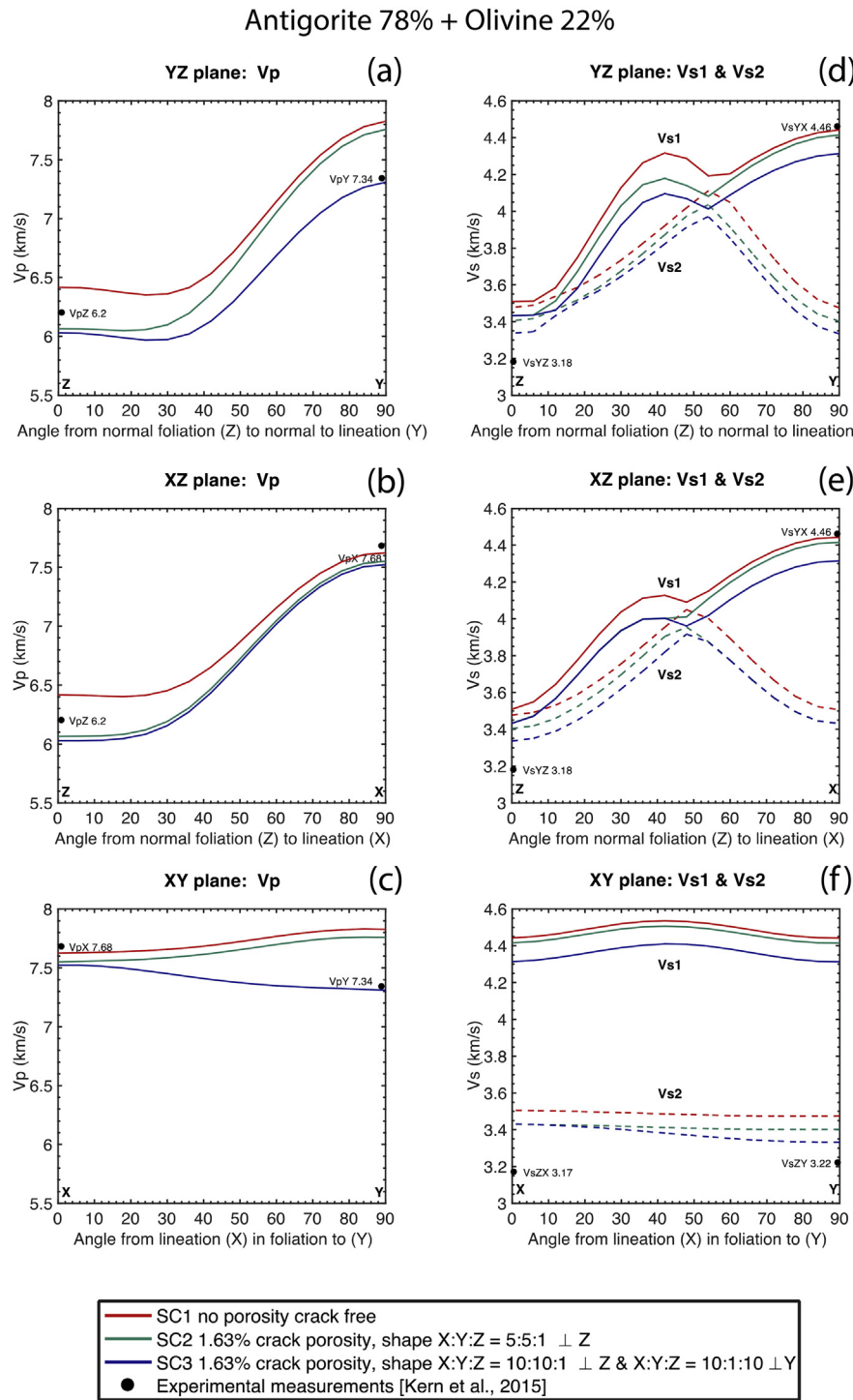
Fig. 4. Effect of crack porosity, shape, and orientation on the seismic velocities of aggregates with 78% antigorite and 22% olivine in the YZ, XZ, and XY planes (a–c) for *Vp* and (d–f) for *Vs* (benchmark results for Morales et al.'s (2018) models). SC1 is a crack-free model with no porosity. SC2 has 1.63% porosity with a crack shape of X:Y:Z = 5:5:1. SC3 has 1.63% porosity with crack shapes of X:Y:Z = 10:10:1 and X:Y:Z = 10:1:10. Black dots labelled with phase velocities indicate experimental measurements (Kern et al., 2015).

are completely lacking for a number of important crustal minerals, including feldspars, amphiboles, micas, and many accessory minerals. Most of the high T-P data are available for minerals in the uppermost mantle, such as olivine, pyroxene, and garnet (Almqvist and Mainprice, 2017). If given the appropriate single-crystal temperature and pressure derivatives, seismic velocities can be simulated using EMT for the in-situ state at high T-P conditions for samples where the microstructure has been changed by subsequent chemical alteration (e.g., the

transformation of olivine to serpentine) or mechanically induced changes (e.g., cracks opened due to decompression) (Mainprice, 1997). EMT can also be used to model some features, such as the presence of fluids (e.g., magma), which are not necessarily preserved in the recovered microstructure (Jousselin and Mainprice, 1998; Lamoureux et al., 1999; Lee et al., 2017; Mainprice, 1997) as well as the effect of phase transformations on the physical properties of rocks (Morales et al., 2018).
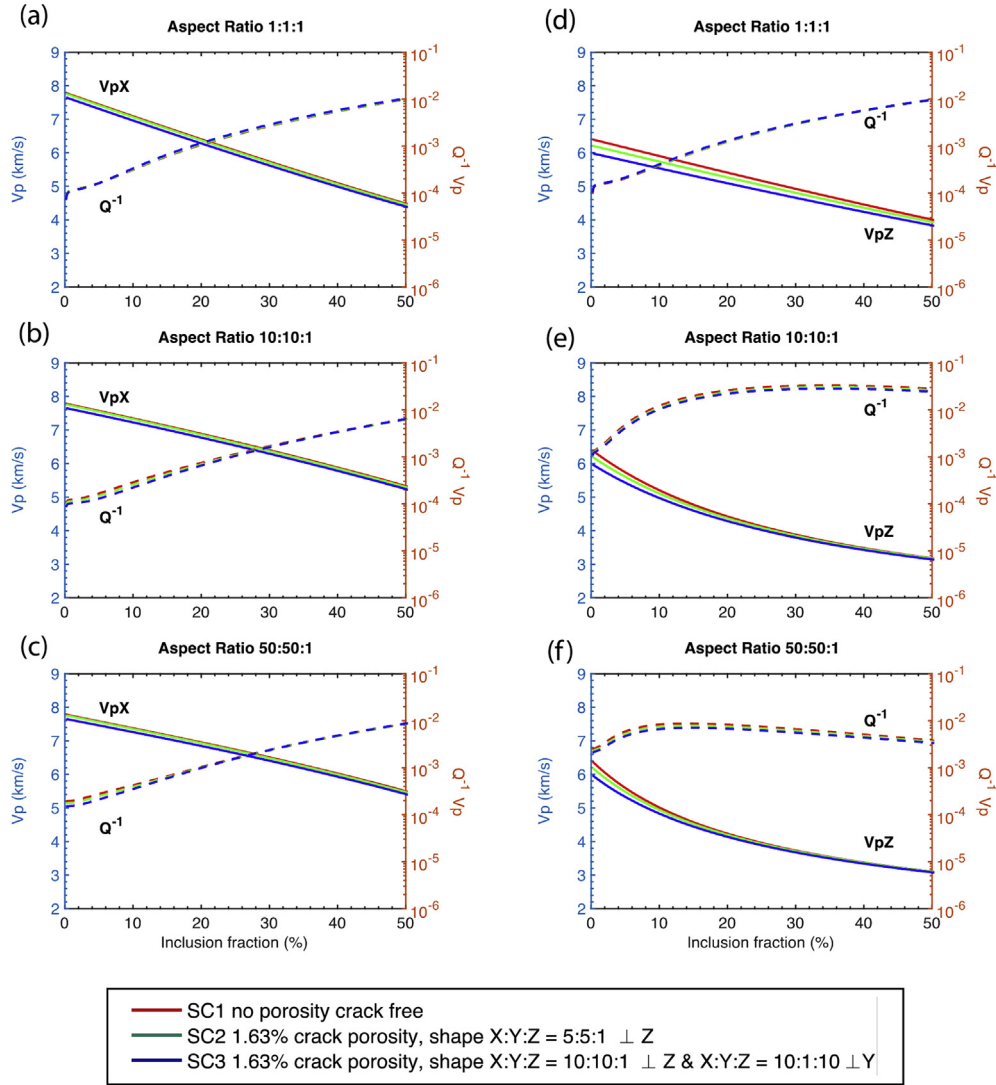
Melt inclusion

Fig. 5. DEM results for the background media of models SC1, SC2, and SC3 with increasing melt inclusion. The Vp and Q^{-1} variations (a–c) in the X direction and (d–f) in the Z direction are plotted for aspect ratios (X/Z) of 1, 10, and 50.

3. Modeling schemes

In this section, we describe Eshelby's (1957) solution used for numerical evaluation of the elastic field of an ellipsoidal inclusion in an infinite medium. The SC scheme used for a background medium, the DEM theory for a porous effective medium, Gassmann's (1951) poroelastic relationship, and the attenuation estimation are also described.

3.1. Eshelby's (1957) Solution

Based on the observation that elastic ellipsoidal inclusions in an infinite medium have uniform stress and strain at all points inside the inclusion, Eshelby (1957) developed analytical techniques for calculating the elastic field of an ellipsoidal inclusion in an isotropic medium. Eshelby's (1957) formula is useful for the study of the mechanical properties of solids, such as precipitations, inclusions, voids, and cracks (Mura, 1987). Kinoshita and Mura (1971) extended Eshelby's (1957) formula to an anisotropic background. The uniform elastic strain tensor inside the inclusion (ε_{ij}) given by Mura (1987) is as follows:

$$\varepsilon_{ij} = \frac{1}{2}(G_{ikjl} + G_{jkil})C_{klmn}\varepsilon_{mn}^* \tag{1}$$

where G_{ikjl} is the tensor Green's function associated with displacement due to a unit force applied in a given direction, C_{klmn} is the elastic stiffness tensor of the background medium, and ε_{mn}^* is the eigenstrain or stress-free strain tensor due to the imaginary removal of the inclusion from the constraining matrix. The symmetrical tensor Green's function G_{ikjl} is given by Mura (1987), and is as follows:

$$G_{ikjl} = \frac{1}{4\pi}\int_0^\pi \sin\theta d\theta \int_0^{2\pi}(K_{ij}^{-1}(x)x_kx_l)d\theta \tag{2}$$

where $K_{ij}(x) = C_{ikjl}x_kx_l$ is the Christoffel stiffness tensor for direction (x) with $x_1 = \sin\theta\cos\phi/a_1$, $x_2 = \sin\theta\sin\phi/a_2$ and $x_3 = \cos\theta/a_3$. The angles θ and ϕ are the spherical coordinates that define the vector x with respect to the principal axes of the ellipsoidal inclusion. The semi-axes of the ellipsoid are given by a_1, a_2, and a_3. The integration to obtain the tensor Green's function should be done numerically, as no analytical solutions exist for a general triclinic elastic background medium (Mainprice, 1997). To improve numerical efficiency, in particular for inclusions with large aspect ratios, we use the Fourier transform of G_{ikjl} and take advantage of the symmetry of the tri-axial ellipsoid to reduce

Model SC3
Inclusion: Melt vs. Water
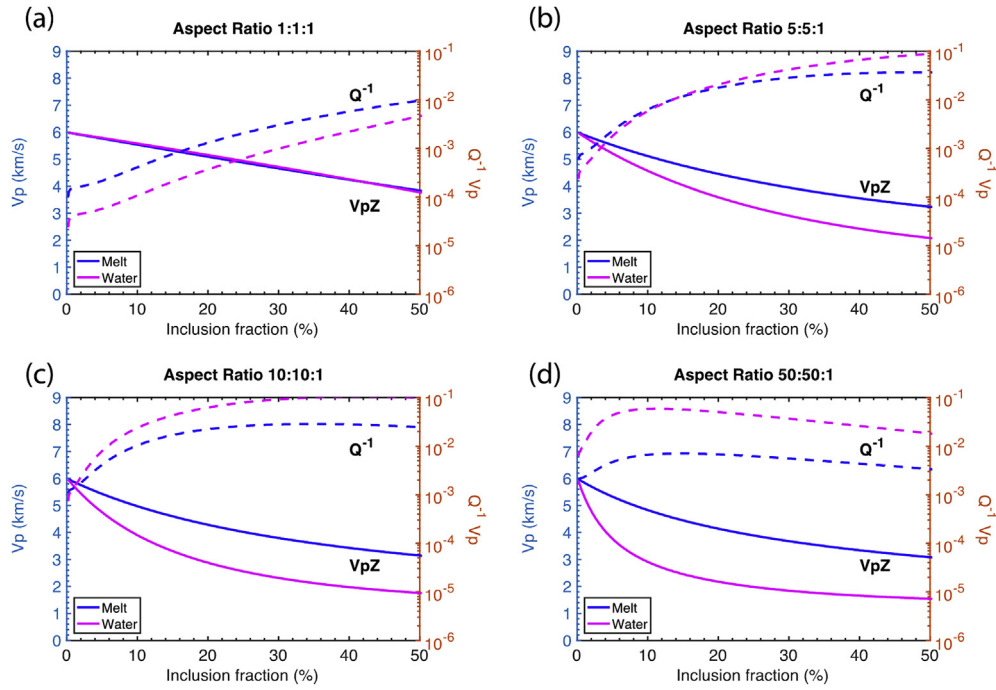
Fig. 6. Comparison of the Vp and Q^{-1} variations in the Z direction between melt and water inclusions. The background medium is the SC3 model, and the ellipsoidal inclusions of melt or water have aspect ratios (X/Z) of (a) 1, (b) 5, (c) 10, and (d) 50.

the amount of integration (Barnett, 1972).

3.2. Self-consistent (SC) scheme

The SC approximation was introduced by Hill (1965) and Budiansky (1965) to account for the interaction between inclusions in non-dilute concentrations. The SC method is based on the introduction of elastic inclusions (e.g., grains, cracks, etc.) into a background matrix, which is estimated using the average elastic tensor of all the crystals in the aggregate. In this method, all components are treated equally, with no material serving as the host (Berryman and Berge, 1993), which means that each component is treated as an inclusion in the anisotropic homogeneous background medium. We use the observed grain shape as the geometry of the inclusions in the SC method (Mainprice, 1997; Morales et al., 2013, 2018). For numerical calculations on the composites consisting of n distinct types of inclusions, we use the scheme proposed by Willis (1977) in which a strain ratio (A_i) is introduced to relate the strains from inside and outside the inclusions, as follows:

$$A_i = [I + G(C_i - C^{SC})]^{-1}. \tag{3}$$

Here, I is the 4th-rank unit tensor $I_{ijkl} = 1/2(\delta_{ik}\delta_{jl} + \delta_{il}\delta_{jk})$, δ_{ik} is the Kronecker delta, G is the symmetrical 4th-rank tensor Green's function, C_i is the elastic stiffness tensor of the ith inclusion, and C^{SC} is the SC solution for the aggregate. The effective elastic constants (C^*) obey the volume (V)-averaged Hooke's law, as follows:

$$C^* \approx C^{SC} = \sigma\varepsilon^{-1} \tag{4}$$

with the stress $\sigma = 1/V\int \sigma(x)dV$ and the strain $\varepsilon = 1/V\int \varepsilon(x)dV$. Using the strain ratio of A_i, the ensemble averages of stress σ^{SC} and strain ε^{SC} can be defined as follows:

$$\sigma^{SC} = \sum_{i=1}^{i=n} V_i C_i A_i \tag{5}$$

$$\varepsilon^{SC} = \sum_{i=1}^{i=n} V_i A_i \tag{6}$$

$$C^{SC} = \sigma^{SC}\varepsilon^{SC-1}. \tag{7}$$

Because the solution for C^{SC} occurs on both sides of the equation, C^{SC} is obtained by iteration (Mainprice, 1997).

3.3. Differential effective medium (DEM) theory

We use the DEM method to study the effects of shapes and volume fraction of the inclusions on seismic properties of a composite composed of a background medium and inclusions. Although the SC approximation is useful for materials that have a significant interaction between inclusions, it progressively overestimates the interaction as the concentration of inclusions increases, showing negative values for Young's modulus and bulk and shear moduli, and Poisson's ratio > 0.5 for saturated cracks at sufficiently high crack densities (Bruner, 1976). The DEM theory was proposed as an alternative differential method in which the inclusion concentration is increased in small steps with a re-evaluation of the elastic constants at each volume fraction, allowing the potential energy of the medium to vary slowly with inclusion concentration (Bruner, 1976). In the DEM theory, the effective interaction between inclusions can be considered negligible, and thus we use the basic inclusions theory of Eshelby (1957), assuming a dilute inclusion concentration, to take into account the interaction (Mainprice, 1997).

DEM modeling is performed by incrementally adding inclusions with a constant aspect ratio to the background medium, and then re-calculating the new effective medium tensor at each volume fraction to construct the two-phase composite model for different volume fractions of inclusions, from 0% to 100%. Following the anisotropic seismic property calculations and numerical methods by Mainprice (1997), we use the equations for DEM tensor (C^{DEM}) derived by McLaughlin (1977):

Harzburgite - Basalt (liquid)
Effect of aspect ratio
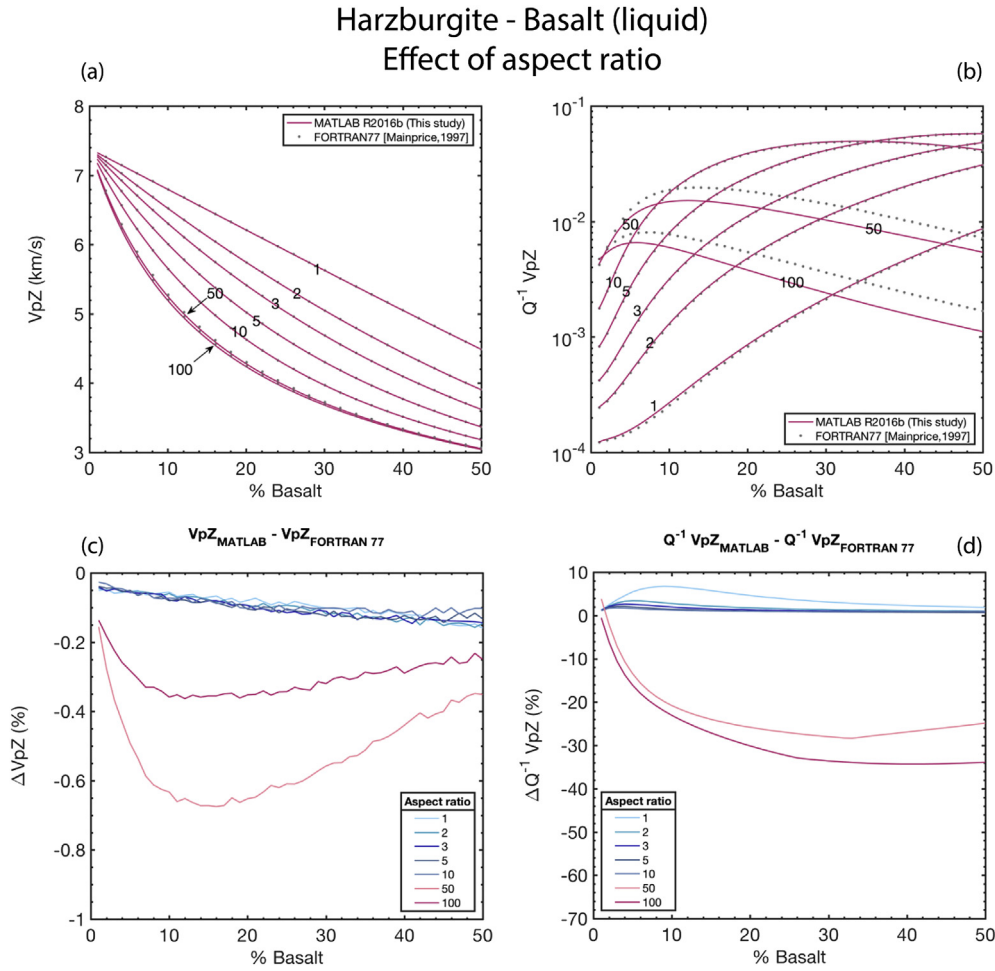
Fig. 7. Comparison of the effect of the inclusion aspect ratio on the DEM results for a harzburgite-basalt (liquid) composite from this study (MATLAB), with previous results from Mainprice (1997) (FORTRAN77). (a) Vp for the Z-axis direction (VpZ). (b) Vp Q^{-1} for the Z-axis direction ($Q^{-1}Vp$Z). The discrepancies in (c) VpZ and (d) $Q^{-1}Vp$Z between MATLAB and FORTRAN77 results.

$$\frac{dC^{DEM}}{dV} = \frac{1}{(1-V)}(C_i - C^{DEM})A_i \tag{8}$$

where the term A_i is the strain concentration factor described in Section 3.2, and V is a volume fraction (proportion). The values C_i and C^{DEM} are the elastic stiffness tensors of the ith inclusion and the effective background medium, respectively. To evaluate the elastic moduli (C^{DEM}) at a given V, the starting value of C^{DEM} and which component is the inclusion must be specified. To ensure accuracy, we use a small volume fraction increment of $dV = 10^{-3}$.

3.4. Gassmann's (1951) Poroelastic relationship

Seismic frequency for a fluid-filled rock can be divided into two ranges of low and high frequency (Le Ravalec and Guéguen, 1996; Mavko, 1980; Mukerji and Mavko, 1994; Schmeling, 1985). The low-frequency range corresponds to a regime where the pore fluid has enough time to reach an equilibrium pore fluid pressure throughout the aggregate, indicating that the pore fluid system is mechanically connected (Mainprice, 1997). In contrast, at high frequency, there is not enough time available for the pore fluid pressure to be the same everywhere, and so the pore fluid system is considered mechanically isolated (Mainprice, 1997). All the SC and DEM schemes as well as Hudson's (1981) method use idealized ellipsoidal inclusions, and hence correspond to the high-frequency case (Mukerji and Mavko, 1994). The low-frequency case can be evaluated using Gassmann's (1951) formula that is a poroelastic relationship between the elastic moduli of a porous

medium with saturated fluid-filled pores and the moduli of the same medium with empty pores. We use Gassmann's (1951) poroelastic relationship extended to anisotropic media by Brown and Korringa (1975), which is given in terms of compliances for a homogeneous material as follows:

$$S_{ijkl}^{sat} = S_{ijkl}^{dry} - \left[\frac{(S_{ijkk}^{dry} - S_{ijkk}^{solid})(S_{iikl}^{dry} - S_{iikl}^{solid})}{(S_{iikk}^{dry} - S_{iikk}^{solid}) + \left(\frac{1}{K_f} - S_{iikk}^{solid}\right)\phi} \right] \tag{9}$$

where the superscripts of "sat", "dry", and "solid" indicate the saturated rock, dry porous medium, and solid mineral components, respectively. The value K_f is the bulk modulus of the pore fluid, and ϕ is the porosity or volume fraction of pore fluid. S^{dry} and S^{solid} are evaluated using the DEM model, after which S^{sat} is calculated (Mainprice, 1997).

3.5. Attenuation

We assume that attenuation in the effective medium is associated with the interaction of pore fluids with the solid rock, rather than absorption within the rock or liquid (Jones, 1986; Mainprice, 1997). We also assume that the medium is a linear viscoelastic body that has the mechanical behavior of the standard linear solid with a single relaxation time, and that the energy loss mechanism is melt squirt (Schmeling, 1985); thus, solid-state mechanisms are ignored (Mainprice, 1997). Based on these two assumptions, a high-frequency modulus (M_h) can be defined from the DEM model and a low-frequency

Harzburgite - Basalt (liquid)
Effect of fluid compressibility (Bf) on Q^{-1} VpZ
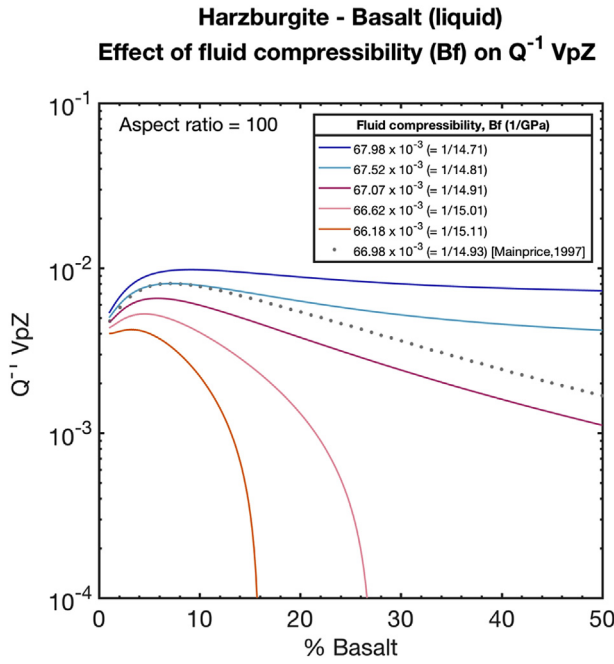
Fig. 8. Effect of fluid compressibility (Bf) on $Q^{-1}VpZ$. Bf is the reciprocal of fluid bulk modulus (Kf). For each Kf, from 14.71 GPa to 15.11 GPa, with an increasing gap of 0.1 GPa, the fluid compressibility is calculated and used to estimate $Q^{-1}VpZ$. For comparison, Mainprice's (1997) result, which was obtained using Kf = 14.93 GPa, is also plotted as gray dots. The background medium and fluid inclusions are harzburgite and liquid basalt, respectively. The aspect ratio of fluid inclusion is 100.

modulus (M_l) can be defined from Gassmann's (1951) formula as well as the DEM model (Mainprice, 1997). The elastic moduli (M) in a given propagation direction (x) are calculated by $M(x) = \rho V(x)^2$ from the phase velocity $V(x)$ and the density (ρ). The maximum amplitude of the Debye attenuation peak is estimated using an equation given by:

$$Q_{max}^{-1} = \frac{M_h - M_l}{q\sqrt{M_h \cdot M_l}} \tag{10}$$

where we use $q = 2$ for the peak attenuation frequency of the relaxation time that is related to the crack aspect ratio that contributes most to the attenuation, fluid viscosity, and rock stiffness (Jones, 1986).

4. Examples

Since DEM models a two-phase composite, the information regarding phase A (e.g., background medium) and phase B (e.g., inclusion) is required as input data. The elastic stiffness tensor (or the velocity and density) is required for both the background medium and inclusion phases. The fluid compressibility (or 1/bulk modulus) of the inclusion is required to calculate Gassmann's (1951) poroelastic

relation and then Q_{max}^{-1}.

4.1. Background medium

We use antigorite-bearing olivine as a background medium to model the effect of fluid on the seismic properties of antigorite. The elastic stiffness tensor of the background rock is calculated using the SC scheme based on the microstructures of antigorite-rich rocks from Val Malenco, Northern Italy (Kern et al., 2015; Morales et al., 2018), which are related to the hydrated subcontinental mantle of the Adriatic lithosphere (Trommsdorff et al., 1993). We use an average composition of 78% antigorite and 22% olivine for the aggregate (Morales et al., 2018). The crystallographic orientations, volume fractions, and the elastic constants of antigorite (Bezacier et al., 2010; Morales et al., 2018) and olivine (Abramson et al., 1997) are used for the SC modeling.

For the end-member background media, we construct three SC models using antigorite and olivine (Morales et al., 2018); (i) SC1, crack-free model of 78% antigorite and 22% olivine with spherical grains; (ii) SC2, 1.63% porosity model of SC1 having cracks with planes normal to the Z-axis, with a crack shape of X:Y:Z = 5:5:1 that is aligned with the foliation plane; and (iii) SC3, 1.63% porosity model of SC1 having two types of crack, one normal to the Z-axis and the other normal to the Y-axis, with shapes X:Y:Z = 10:10:1 and X:Y:Z = 10:1:10, respectively (Kern et al., 2015; Morales et al., 2018).
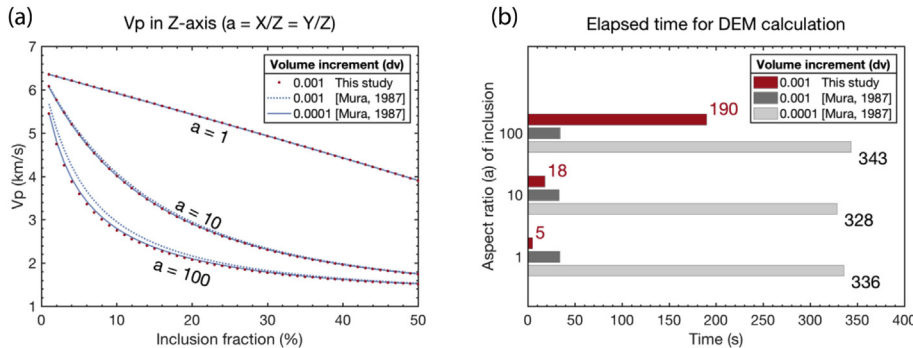
4.2. Inclusion

For the inclusion phase, we assume that cracks in the background medium are filled with water or liquid basalt (melt). The shape of the cracks is assumed to be a sphere (aspect ratio = X/Z = 1) or ellipsoid (aspect ratio = X/Z = 10 or 50). The symmetry axis of ellipsoidal cracks is aligned parallel to the Z-axis. For the isotropic elastic tensor of the melt, the bulk modulus (K_f) is derived from the compressibility ($B_f = 1/K_f$) data at 1200 °C of Murase and McBirney (1973). For the isotropic elastic tensor of water, the bulk modulus is derived from $Vp = 1.483$ km/s and $Vs = 0$ km/s at a temperature of 25 °C.

4.3. GassDem GUI

GassDem graphical user interface (GUI) is designed using the MATLAB (R2016b) App Designer to provide a flexible tool for parameter selection and for the calculation of elastic stiffness tensor of porous effective medium with fluid inclusions based on the DEM theory and Gassmann's (1951) poroelastic relationship (Fig. 1). The structure of GassDem GUI is four main tabs (Effective Medium, Inclusion Shape and Orientation, DEM Analysis, and Help) and four sub-tabs under the Help tab (About GassDem, Inputs, Outputs, and Codes). A default data set (Figs. 1–3) is an example of background and inclusion phases described in Sections 4.1 and 4.2 for the user to replicate DEM modeling (see user manual for further information).

In the Effective Medium tab (Fig. 1), the user can construct a two-

Fig. 9. Comparison of the *Vp* and elapsed time for DEM processing, from both this study and Mura (1987), using each inclusion with an aspect ratio of 1, 10, and 100. (a) *Vp* variations in the Z-axis direction with increasing inclusion volume fraction. (b) Elapsed times for calculating the tensor equation of DEM according to the aspect ratio.
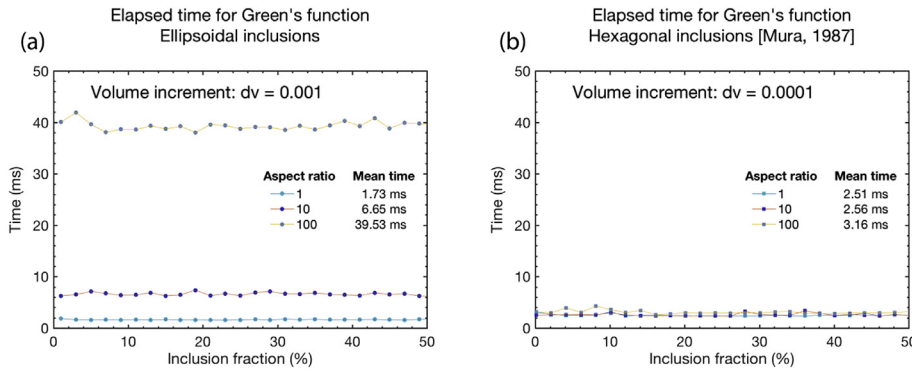
Fig. 10. Elapsed times for calculating Green's function according to aspect ratios of 1, 10, and 100. (a) Calculation from this study using Green's function Fourier integrals at each volume fraction with an increment of 0.001. (b) Calculation from Mura's (1987) method, using the non-zero components of Green's function tensor for hexagonal inclusions at each volume fraction with an increment of 0.0001.

component system of phases A and B that are set as the host medium and inclusion (e.g., fluid), respectively. The user can specify the name, elastic constants file (*.txt), and density (g/cm³) of two phases. The elastic constants file should contain the Voigt elastic stiffness matrix in GPa (see user manual for the input format of elastic constants file). The full paths of directories of input files and GassDem codes are required. The fluid properties of compressibility (1/GPa), viscosity (Pa·s), Vp (km/s), and density (g/cm³) are the input parameters for Gassmann's relationship and attenuation estimation. Note that the bulk modulus of fluid inclusion should be consistent with fluid compressibility (or 1/bulk modulus) in the Fluid properties panel because the fluid compressibility B_f is the reciprocal of bulk modulus K_f ($B_f = 1/K_f$) and is a crucial factor in calculating Q_{max}^{-1}. The maximum % error for Green's Tensor is required (e.g., 0.1).

In the Inclusion Shape and Orientation tab (Fig. 2), the user can select the shape and define the orientation of inclusion. For the inclusion shape, the user can select a sphere or an ellipsoid. If a sphere is selected, the semi-axes lengths are set to be A1:A2:A3 = 1:1:1. If an ellipsoid is selected, the user should specify semi-axes lengths (e.g., A1:A2:A3 = 5:5:1). The orientation of shape ellipsoid semi-axes can be set to be parallel to the elastic tensor axes or parallel to the user-defined orientation (shape preferred orientation, SPO). If the user selects an orientation that is parallel to elastic tensor axes, the ellipsoid semi-axes (A) are parallel to elastic tensor axes (X). For example, A1//X1, A2//X2, and A3//X3 are set for olivine with the principal axes X1 = [100], X2 = [010], and X3 = [001]. If the user selects an orientation that is parallel to user-defined orientation, the azimuth (°) and inclination (°) are required for A1 and A3. Note that A1 should be 90° to A3, which can be checked by the user (see user manual for further information of orientation).

In the DEM Analysis tab (Fig. 3), the file name and directory are required to save DEM results. A filename extension should not be contained in the file name that will be used as a prefix to save outputs as text files (*.txt) in the program. The maximum volume fraction of inclusion for DEM processing can be specified between 0 and 1. The Current status panel shows the name of inclusion, volume fraction increment step size (dVb) and total steps, and progress status ("Processing" or "Completed") of the calculation. The Figure configuration panel can be used to plot Vp, Vs, and Q_{max}^{-1} as a function of the inclusion volume fraction by specifying the structural direction X, Y, or Z, which are lineation, normal to the lineation in the foliation plane, or normal to the foliation plane, respectively, as well as the shear-wave direction, which can be fast (Vs_1) or slow (Vs_2).

The user can refer to the Help tab for information about GassDem and several notes on inputs, outputs, and codes (see user manual).

4.4. DEM results

The predicted velocities of the background models SC1, SC2, and SC3 in the YZ, XZ, and XY planes are plotted with the propagation direction, and are compared with the experimental values, indicating that crack porosity and shape significantly affect the seismic velocities (Fig. 4).

DEM results of the Vp and Q_{max}^{-1} variations in X and Z directions with increasing melt fraction are shown for aspect ratios (X/Z) of 1, 10, and 50 (Fig. 5). For Vp in the X direction, the decrease in velocity with increasing melt fraction shows a similar pattern for aspect ratios of 1, 10, and 50 in all models; SC1, SC2, and SC3 (Fig. 5a–c). For the Z direction, the differences in Vp between the background models SC1, SC2, and SC3 decrease as the aspect ratio increases from 1 to 50 (Fig. 5d–f). This result indicates that the elastic property of a background medium is crucial in determining values of melt fraction that are less than 0.5.

In Fig. 6, variations of Vp and attenuation (Q_{max}^{-1}) in the Z direction are compared between melt and water inclusions at aspect ratios of 1, 5, 10, and 50 for the SC3 background model. For spherical inclusions, the effect of water-filled cracks on the decrease in Vp is similar to that of melt (Fig. 6a), whereas it is stronger than that of melt for ellipsoidal inclusions when the aspect ratio > 1, showing a significant decrease in Vp for the volume fraction < 0.2 (Fig. 6b–d). For spherical inclusions, Q_{max}^{-1} of water is lower than that of melt at all volume fractions (Fig. 6a), whereas it becomes higher than that of melt as the aspect ratio increases from 5 to 50 (Fig. 6b–d). Wepfer and Christensen (1991) showed that the Q values are significantly affected by the confining pressure in ophiolite samples due to the influence of cracks. Considering the relationship between seismic velocity and crack property, it is inferred that the inclusion shape and fluid type (or fluid bulk modulus) may significantly affect the seismic attenuation as well as velocity.

5. Discussion

5.1. Improvements in computing for GassDem

To check whether results from this MATLAB program are consistent with those from the FORTRAN77 program by Mainprice (1997), we recalculate seismic properties of mid-ocean ridge rocks using Mainprice's (1997) examples. For anisotropic effective media with harzburgite modal composition and crystallographic preferred orientation at 1200 °C and 200 MPa, the ellipsoidal inclusions of liquid basalt (melt) with aspect ratios ranging from 1 to 10 result in the same Vp for the Z-axis direction (VpZ) as Mainprice's (1997) results (Fig. 7a). However, for large aspect ratios of 50 and 100, the VpZ values at melt volume fraction of ~0.15 are lower by ~0.70% and ~0.35%, respectively, than those of Mainprice (1997) (Fig. 7c). The Vp attenuation for the Z-axis ($Q^{-1}VpZ$) is also similar to Mainprice's (1997) results for aspect ratios between 1 and 10 (Fig. 7b), whereas it is lower by ~25% and ~34% for aspect ratios of 50 and 100, respectively, than Mainprice's (1997) results when the volume fraction of melt is above ~0.15 (Fig. 7d). Although there is a slight decreasing trend in ΔVpZ (difference in the results between Mainprice (1997) and this study) for aspect ratios less than 10 (Fig. 7c), $\Delta Q^{-1}VpZ$ is almost zero (Fig. 7d). This indicates that the decreasing trend in ΔVpZ results from an improvement in the computing platform (from FORTRAN77 32-bit to MATLAB 64-bit). The

significant discrepancy in $Q^{-1}Vp$Z may be related to a large uncertainty associated with the estimate of attenuation. When we test the effect of fluid compressibility (B_f) on $Q^{-1}Vp$Z, there is a substantial variation in $Q^{-1}Vp$Z due to a very small change in B_f (Fig. 8). Because the estimation of $Q^{-1}Vp$Z is based on the DEM results for fluid-filled rocks and fluid-unfilled rocks, as well as Gassmann's (1951) poroelastic relation, the B_f value for Gassmann's (1951) equation should be consistent with the inverse of bulk modulus of fluid inclusion used for the DEM calculation. For the example shown in Fig. 7, B_f is 67.07×10^{-3}, which is the inverse of bulk modulus (1/14.91 GPa) of fluid inclusion. If the B_f value of 66.62×10^{-3} (1/GPa) is used, which is derived from the bulk modulus of 15.01 GPa that is slightly larger than that of fluid inclusion (14.91 GPa), $Q^{-1}Vp$Z abruptly decreases to 0.0001 as melt volume fraction increases to ~ 0.265. A variation of only 0.45×10^{-3} (1/GPa) can cause this substantial change in attenuation. Although the sensitivity of $Q^{-1}Vp$Z to B_f limits the evaluation of attenuation, our results indicate that the DEM theory combined with Gassmann's relationship can be used to predict attenuation in the effective medium with fluid-filled inclusions. Most of the studies using EMT have modeled the seismic properties of fluid inclusions in rocks with no evaluation of the attenuation (e.g., Taylor and Singh, 2002).

5.2. Kelvin tensor notation

The 4th-rank tensor (C_{ijkl}) is traditionally transformed to the Voigt matrix (C_{ij}) according to the following rules: $11 \rightarrow 1$; $22 \rightarrow 2$; $33 \rightarrow 3$; $23, 32 \rightarrow 4$; $13, 31 \rightarrow 5$; $12, 21 \rightarrow 6$, based on the symmetries of the stiffness tensor (Dellinger et al., 1998). Although the Voigt notation is convenient because each element of matrix C_{ij} is equal to its corresponding element in the tensor C_{ijkl}, it does not preserve the norm that is a sum of the squares of the elastic tensor elements having geometrical significance (Dellinger et al., 1998) as follows:

$$\sum_{i,j} C_{ij}^2 \neq \sum_{i,j,k,l} C_{ijkl}^2 \quad : \text{Voigt notation.} \tag{11}$$

A slightly different normalization form of "Kelvin notation", which was originally introduced as "EigenTensor" by Lord Kelvin (Thomson) (1856), preserves the tensor norm (Helbig, 1994) as follows:

$$\sum_{i,j} C_{ij}^2 = \sum_{i,j,k,l} C_{ijkl}^2 \quad : \text{Kelvin notation.} \tag{12}$$

Hence, the Kelvin notation transfers the tensor algebra of elasticity from 4th-rank tensors to 2nd-rank tensors. This has some advantages, for instance, the rotations of elastic stiffness [C] and elastic compliance [S] are performed in the same way, unlike with the Voigt notation (Mehrabadi and Cowin, 1990).

To calculate the tensor equation of DEM (Equation (8)), we use the simple Euler method (Courtemanche et al., 1993) given as

$$C^{DEM}(Vb + dVb) = C^{DEM}(Vb) + \frac{dVb}{(1 - Vb)}(C_i - C^{DEM}(Vb))A_i. \tag{13}$$

Here, Vb is the current volume fraction of inclusion and dVb is the volume fraction increment. To calculate $(C_i - C^{DEM}(Vb))A_i$, we convert each Voigt matrix into a Kelvin matrix by performing pre- and post-multiplication of the scaling matrix given as

$$\begin{bmatrix} 1 & 0 & 0 & 0 & 0 & 0 \\ 0 & 1 & 0 & 0 & 0 & 0 \\ 0 & 0 & 1 & 0 & 0 & 0 \\ 0 & 0 & 0 & \sqrt{2} & 0 & 0 \\ 0 & 0 & 0 & 0 & \sqrt{2} & 0 \\ 0 & 0 & 0 & 0 & 0 & \sqrt{2} \end{bmatrix} \tag{14}$$

and then the Kelvin matrix of $C^{DEM}(Vb + dVb)$ is converted back into a Voigt matrix by performing pre- and post-multiplication of the inverse of the scaling matrix.

5.3. Tensor Green's function fourier integral

Most of the previous studies have used the method of Mura (1987), in which the Voigt matrix is used to calculate the non-zero components of Green's function $\bar{G}_{ijkl}$, and then the Runge-Kutta method is used to calculate the DEM equation (e.g., Jakobsen et al., 2000; Seher et al., 2010; Taylor and Singh, 2002). Because Mura (1987) considered some special cases of spheroids (a1 = a2, a1/a3 = p), cylinders ($a_3 \rightarrow \infty$) (elliptic inclusions) and flat ellipsoids ($a_3 \rightarrow 0$), and the crystalline directions are assumed to be coincident with the principal directions of the spheroid [p. 137 in Mura (1987)], there exist limits regarding the modeling of rocks with various shapes and orientations.

We use volume fraction increment of 0.001 for DEM. The Vp variations in the Z-axis show that as the aspect ratio increases to 100, the results are more consistent with those from Mura's (1987) method using a volume fraction increment of 0.0001 rather than 0.001 (Fig. 9a). This indicates that our method is more efficient than Mura's (1987) method because the volume fraction increment of 0.0001 requires an elapsed time that is 10 times longer than the volume fraction increment of 0.001 in Mura's (1987) method (Fig. 9b). As a result, our DEM processing in the MATLAB program requires only 5 s for spherical inclusions, whereas Mura's (1987) method requires 336 s to obtain the same result (Fig. 9b). For ellipsoidal inclusions with an aspect ratio of 100, the elapsed time is also 45% faster than Mura's (1987) method (Fig. 9b). The mean values of elapsed times for calculating the Green's function Fourier integrals at each volume fraction with an increment of 0.001 are 1.73, 6.65, and 39.53 ms for aspect ratios of 1, 10, and 100, respectively (Fig. 10a). Although the elapsed times for ellipsoidal inclusions with aspect ratios of 10 and 100 are slower than the corresponding elapsed times of 2.56 and 3.16 ms obtained from Mura's (1987) method (Fig. 10b), the Green's function Fourier integrals, combined with the simple Euler method, is more efficient to calculate the entire DEM equation.

6. Summary

In this study, a combination of the SC and DEM theories as well as the poroelastic relationship of Gassmann (1951) are used to model the seismic velocity and anisotropy of the effective medium, and then to verify the effects of the geometry and bulk modulus of fluid inclusions on the seismic properties. The algorithm of the modeling scheme presented here is based on the FORTRAN77 code of Mainprice (1997). The SC scheme for creating end-member background media is implemented in FORTRAN77. For the DEM modeling, we have translated Mainprice's (1997) FORTRAN77 code into a MATLAB program (GassDem), and then used it to calculate the elastic stiffness, seismic velocity, and maximum quality factor (Q_{max}^{-1}) of a composite comprised of a background medium and inclusions. GassDem GUI is designed to provide a user-friendly program, and it is publicly available online, and details on how to run the program are described in this paper as well as user manual. Several examples are performed to model the elastic properties for the antigorite sample, consisting of antigorite and olivine, and to compare the results with the real data. The effect of the volume fraction of fluid-filled cracks, such as water and liquid basalt, and the effects of the crack shape and fluid type on the seismic velocities are investigated. Our results obtained from the examples indicate that the microstructure of the rock and the bulk modulus and shape of fluid are crucial in predicting the seismic properties. More reliable predictions of the seismic velocities can improve the interpretation of seismic velocity anomaly zones and/or the estimation of the volume fraction of fluid in low-velocity zones.

Computer code availability

The source code, example input data, and user manual are available at https://github.com/ekim1419/GassDem.

Acknowledgements

References

Abramson, E.H., Brown, J.M., Slutsky, L.J., Zaug, J., 1997. The elastic constants of San Carlos olivine to 17 GPa. J. Geophys. Res.: Solid Earth 102 (B6), 12253–12263. https://doi.org/10.1029/97JB00682.

Almqvist, B.S.G., Mainprice, D., 2017. Seismic properties and anisotropy of the continental crust: predictions based on mineral texture and rock microstructure. Rev. Geophys. 55 (2), 367–433. https://doi.org/10.1002/2016RG000552.

Anderson, D.L., Minster, B., Cole, D., 1974. The effect of oriented cracks on seismic velocities. J. Geophys. Res. 79 (26), 4011–4015. https://doi.org/10.1029/JB079i026p04011.

Arnulf, A.F., Singh, S.C., Harding, A.J., Kent, G.M., Crawford, W., 2011. Strong seismic heterogeneity in layer 2A near hydrothermal vents at the Mid-Atlantic Ridge. Geophys. Res. Lett. 38 (13). https://doi.org/10.1029/2011GL047753.

Barnett, D.M., 1972. The precise evaluation of derivatives of the anisotropic elastic Green's functions. Phys. Status Solidi 49 (2), 741–748.

Barruol, G., Kern, H., 1996. Seismic anisotropy and shear-wave splitting in lower-crustal and upper-mantle rocks from the Ivrea Zone—experimental and calculated data. Phys. Earth Planet. In. 95 (3), 175–194. https://doi.org/10.1016/0031-9201(95)03124-3.

Berryman, J.G., Berge, P.A., 1993. Rock elastic properties: dependence on microstructure. In: Proceedings of the Symposium on Homogenization and Constitutive Modeling for Heterogeneous Materials, American Society of Mechanical Engineers - Applied Mechanics Division, Symposium on Homogenization and Constitutive Modeling for Heterogeneous Materials. University of Virginia, Charlottesville, Virginia, pp. 1–13.

Bezacier, L., Reynard, B., Bass, J.D., Sanchez-Valle, C., Van de Moortèle, B., 2010. Elasticity of antigorite, seismic detection of serpentinites, and anisotropy in subduction zones. Earth Planet. Sci. Lett. 289 (1), 198–208. https://doi.org/10.1016/j.epsl.2009.11.009.

Brown, R.J.S., Korringa, J., 1975. On the dependence of the elastic properties of a porous rock on the compressibility of the pore fluid. Geophysics 40 (4), 608–616. https://doi.org/10.1190/1.1440551.

Bruner, W.M., 1976. Comment on 'Seismic velocities in dry and saturated cracked solids' by Richard J. O'Connell and Bernard Budiansky. J. Geophys. Res. 81 (14), 2573–2576. https://doi.org/10.1029/JB081i014p02573.

Budiansky, B., 1965. On the elastic moduli of some heterogeneous materials. J. Mech. Phys. Solid. 13 (4), 223–227. https://doi.org/10.1016/0022-5096(65)90011-6.

Carlson, R.L., Gangi, A.F., 1985. Effect of cracks on the pressure dependence of P wave velocities in crystalline rocks. J. Geophys. Res.: Solid Earth 90 (B10), 8675–8684. https://doi.org/10.1029/JB090iB10p08675.

Courtemanche, M., Glass, L., Keener, J.P., 1993. Instabilities of a propagating pulse in a ring of excitable media. Phys. Rev. Lett. 70 (14), 2182.

Crampin, S., 1987. The basis for earthquake prediction. Geophys. J. Int. 91 (2), 331–347. https://doi.org/10.1111/j.1365-246X.1987.tb05230.x.

Dellinger, J., Vasicek, D., Sondergeld, C., 1998. Kelvin notation for stabilizing elastic-constant inversion. Rev. Inst. Fr. Pét. 53 (5), 709–719.

Eshelby, J.D., 1957. The determination of the elastic field of an ellipsoidal inclusion, and related problems. Proc. Roy. Soc. Lond. Math. Phys. Sci. 241 (1226), 376.

Gassmann, F., 1951. Über die elastizität poröser medien. Vierteljahrsschrift der Naturforschenden Gesellschaft Zürich 96, 1–23. (Paper translation at. http://sepwww.stanford.edu/public/docs/sep102/jim2.ps.gz.

Griffiths, L., Heap, M.J., Baud, P., Schmittbuhl, J., 2017. Quantification of microcrack characteristics and implications for stiffness and strength of granite. Int. J. Rock Mech. Min. Sci. 100, 138–150. https://doi.org/10.1016/j.ijrmms.2017.10.013.

Helbig, K., 1994. Foundations of Anisotropy for Exploration Seismics: Handbook of Geophysical Exploration, I: Seismic Exploration. Pergamon Press, Oxford.

Hill, R., 1965. A self-consistent mechanics of composite materials. J. Mech. Phys. Solid. 13 (4), 213–222. https://doi.org/10.1016/0022-5096(65)90010-4.

Hudson, J.A., 1981. Wave speeds and attenuation of elastic waves in material containing cracks. Geophys. J. R. Astron. Soc. 64 (1), 133–150. https://doi.org/10.1111/j.1365-246X.1981.tb02662.x.

Huot, G., Singh, S.C., 2018. Seismic evidence for fluid/gas beneath the Mentawai fore-arc basin, central Sumatra. J. Geophys. Res.: Solid Earth 123 (2), 957–976. https://doi.org/10.1002/2017JB014849.

Jakobsen, M., Hudson, J.A., Minshull, T.A., Singh, S.C., 2000. Elastic properties of hydrate-bearing sediments using effective medium theory. J. Geophys. Res.: Solid Earth 105 (B1), 561–577. https://doi.org/10.1029/1999JB900190.

Jones, T.D., 1986. Pore fluids and frequency-dependent wave propagation in rocks. Geophysics 51 (10), 1939–1953. https://doi.org/10.1190/1.1442050.

Jousselin, D., Mainprice, D., 1998. Melt topology and seismic anisotropy in mantle peridotites of the Oman ophiolite. Earth Planet. Sci. Lett. 164 (3), 553–568. https://doi.org/10.1016/S0012-821X(98)00235-0.

Kern, H., Lokajicek, T., Svitek, T., Wenk, H.-R., 2015. Seismic anisotropy of serpentinite from val Malenco, Italy. J. Geophys. Res.: Solid Earth 120 (6), 4113–4129. https://doi.org/10.1002/2015JB012030.

Kim, E., Toomey, D.R., Hooft, E.E.E., Wilcock, W.S.D., Weekly, R.T., Lee, S.-M., Kim, Y.H., 2019. Upper crustal Vp/Vs ratios at the Endeavour segment, Juan de Fuca Ridge, from joint inversion of P and S travel times: implications for hydrothermal circulation. Geochem. Geophys. Geosyst. 20, 208–229. https://doi.org/10.1029/2018GC007921.

Kinoshita, N., Mura, T., 1971. Elastic fields of inclusions in anisotropic media. Phys. Status Solidi 5 (3), 759–768. https://doi.org/10.1002/pssa.2210050332.

Kranz, R.L., 1983. Microcracks in rocks: a review. Tectonophysics 100 (1), 449–480. https://doi.org/10.1016/0040-1951(83)90198-1.

Lamoureux, G., Ildefonse, B., Mainprice, D., 1999. Modelling the seismic properties of fast-spreading ridge crustal Low-Velocity Zones: insights from Oman gabbro textures. Tectonophysics 312 (2), 283–301. https://doi.org/10.1016/S0040-1951(99)00183-3.

Le Ravalec, M., Guéguen, Y., 1996. High- and low-frequency elastic moduli for a saturated porous/cracked rock-Differential self-consistent and poroelastic theories. Geophysics 61 (4), 1080–1094. https://doi.org/10.1190/1.1444029.

Lee, A.L., Walker, A.M., Lloyd, G.E., Torvela, T., 2017. Modeling the impact of melt on seismic properties during mountain building. Geochem. Geophys. Geosyst. 18 (3), 1090–1110. https://doi.org/10.1002/2016GC006705.

Lord Kelvin (Thomson), W., 1856. Elements of a mathematical theory of elasticity. Phil. Trans. Roy. Soc. Lond. 146, 481–498.

Mainprice, D., 1997. Modelling the anisotropic seismic properties of partially molten rocks found at mid-ocean ridges. Tectonophysics 279 (1), 161–179. https://doi.org/10.1016/S0040-1951(97)00122-4.

Mavko, G.M., 1980. Velocity and attenuation in partially molten rocks. J. Geophys. Res.: Solid Earth 85 (B10), 5173–5189. https://doi.org/10.1029/JB085iB10p05173.

McLaughlin, R., 1977. A study of the differential scheme for composite materials. Int. J. Eng. Sci. 15 (4), 237–244. https://doi.org/10.1016/0020-7225(77)90058-1.

Mehrabadi, M.M., Cowin, S.C., 1990. Eigentensors of linear anisotropic elastic materials. Q. J. Mech. Appl. Math. 43 (1), 15–41. https://doi.org/10.1093/qjmam/43.1.15.

Morales, L.F.G., Mainprice, D., Boudier, F., 2013. The influence of hydrous phases on the microstructure and seismic properties of a hydrated mantle rock. Tectonophysics 594, 103–117. https://doi.org/10.1016/j.tecto.2013.03.022.

Morales, L.F.G., Mainprice, D., Kern, H., 2018. Olivine-antigorite orientation relationships: microstructures, phase boundary misorientations and the effect of cracks in the seismic properties of serpentinites. Tectonophysics 724–725, 93–115. https://doi.org/10.1016/j.tecto.2017.12.009.

Mukerji, T., Mavko, G., 1994. Pore fluid effects on seismic velocity in anisotropic rocks. Geophysics 59 (2), 233–244. https://doi.org/10.1190/1.1443585.

Mura, T., 1987. Micromechanics of Defects in Solids, Second. Martinus Nijhoff, Dordrecht, The Netherlands.

Murase, T., McBirney, A.R., 1973. Properties of some common igneous rocks and their melts at high temperatures. GSA Bulletin 84 (11), 3563–3592. https://doi.org/10.1130/0016-7606(1973)84<3563:POSCIR>2.0.CO;2.

Paterson, M.S., Wong, T.-f., 2005. Experimental Rock Deformation-The Brittle Field. Springer Science & Business Media.

Pio Lucente, F., De Gori, P., Margheriti, L., Piccinini, D., Di Bona, M., Chiarabba, C., Piana Agostinetti, N., 2010. Temporal variation of seismic velocity and anisotropy before the 2009 MW 6.3 L'Aquila earthquake, Italy. Geology 38 (11), 1015–1018.

Schmeling, H., 1985. Numerical models on the influence of partial melt on elastic, anelastic and electric properties of rocks. Part I: elasticity and anelasticity. Phys. Earth Planet. In. 41 (1), 34–57. https://doi.org/10.1016/0031-9201(85)90100-1.

Seher, T., Singh, S.C., Crawford, W.C., Escartín, J., 2010. Upper crustal velocity structure beneath the central Lucky Strike Segment from seismic refraction measurements. Geochem. Geophys. Geosyst. 11 (5). https://doi.org/10.1029/2009GC002894.

Taylor, M.A.J., Singh, S.C., 2002. Composition and microstructure of magma bodies from effective medium theory. Geophys. J. Int. 149 (1), 15–21. https://doi.org/10.1046/j.1365-246X.2002.01577.x.

Trommsdorff, V., Piccardo, G.B., Montrasio, A., 1993. From magmatism through metamorphism to sea floor emplacement of subcontinental Adria lithosphere during pre-Alpine rifting (Malenco, Italy). Schweizerische Mineralogische und Petrographische Mitteilungen 73 (2), 191–203.

Walsh, J.B., 1965. The effect of cracks on the compressibility of rock. J. Geophys. Res. 70 (2), 381–389. https://doi.org/10.1029/JZ070i002p00381.

Wenk, H.-R., Vasin, R.N., Kern, H., Matthies, S., Vogel, S.C., Ivankina, T.I., 2012. Revisiting elastic anisotropy of biotite gneiss from the Outokumpu scientific drill hole based on new texture measurements and texture-based velocity calculations. Tectonophysics 570–571, 123–134. https://doi.org/10.1016/j.tecto.2012.06.023.

Wepfer, W.W., Christensen, N.I., 1991. Q structure of the oceanic crust. Mar. Geophys. Res. 13 (3), 227–237. https://doi.org/10.1007/bf00369151.

Willis, J.R., 1977. Bounds and self-consistent estimates for the overall properties of anisotropic composites. J. Mech. Phys. Solid. 25 (3), 185–202. https://doi.org/10.1016/0022-5096(77)90022-9.